Supporting Information

Hot Exciton Organic Glassy Scintillator for High-Resolution X-ray Imaging

Xi Yang,[a,b] Jingru Chen,[c] Yang Zhang,[c] Yiming Di,[c] Guozhen Zhang,[c] Songhua Chen,[b]* Hongming Chen[a]* and Meijin Lin[a,c]*

a. College of Materials Science and Engineering, Fuzhou University, Fuzhou, 350116, P.R. China. E-mail: chm@fzu.edu.cn; meijin_lin@fzu.edu.cn.

b. College of Chemistry and Material, Longyan University, Longyan, 364000, P. R. China. E-mail: songhua@iccas.ac.cn.

c. College of Chemistry, Fuzhou University, Fuzhou, 350116, P.R. China.

Keywords: Organic glassy scintillator, Hot exciton, Hybridized local and charge-transfer, X-ray imaging

Experimental Section

1. Materials

Chemicals and solvents were obtained from Energy or Innochem and were of reagent grade or higher, used without further purification. Solvents used for chromatography and workup were generally of reagent grade. All reactions were conducted under argon in oven-dried glassware unless otherwise specified. The temperatures for all reactions were measured externally.

Synthesis details
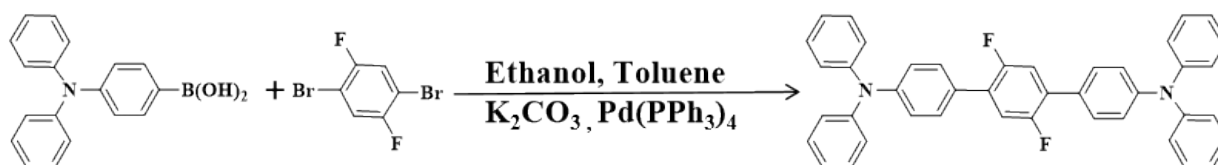
Figure S1. Synthesis route of DTPA2F.

Synthesis 2',5'-difluoro-N4,N4, N4'',N4''-tetraphenyl-[1,1':4',1''-terphenyl]-4,4''-diamine (DTPA2F): in a two-neck round-bottom flask, 1,4-dibromo-2,5-difluorobenzene (2.7g, 10 mmol), (4-(diphenylamino)phenyl) boronic acid (6.36 g, 22 mmol) and tetracids-triphenylphosphine palladium Pd(PPh$_3$)$_4$ (0.58 g, 0.5 mmol) were combined. Subsequently, a 2M potassium carbonate solution (16 mL), ethanol (16 mL), and toluene (50 mL) were added to the flask using syringes. The reaction mixture was refluxed for 24 hours and then allowed to cool to room temperature. The mixture was then extracted three times with dichloromethane, and the combined organic layers were dried over anhydrous magnesium sulfate. After filtration and evaporation, the crude product was further purified by silica-gel column chromatography using dichloromethane/petroleum ether (1/8, v/v) as the eluent. The final product was obtained by recrystallization from a mixed solvent of dichloromethane and ethanol, yielding a white solid (5.2 g, 86% combined yield). ^{1}H NMR (400 MHz, Chloroform-d): δ 7.43-7.48 (d, 4H, Ar H), δ 7.26-7.32 (t, 8H, Ar H), δ 7.18-7.25 (t, 4H, Ar H), δ 7.11-7.17 (t, 12H, Ar H), 7.03-7.09 (t, 4H,

Ar H); ^{13}C NMR (400 MHz, Chloroform-d): δ 157.03, 154.59, 147.83, 147.46, 129.53, 129.38, 128.01, 124.83, 123.33, 122.90, 117.12, 117.00, 116.81.
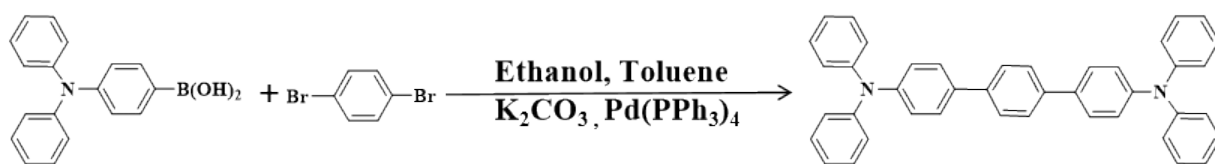
Figure S2. Synthesis route of TPABTPA.

Synthesis of N4, N4, N4'', N4''-tetraphenyl-[1,1':4',1''-terphenyl]-4,4''-diamine (TPABTPA): The compound TPABTPA was synthesized using a procedure similar to that for DTPA2F, with 1,4-dibromobenzene (2.6 g, 11 mmol) substituted for 1,4-dibromo-2,5-difluorobenzene. TPABTPA was obtained as a white solid with a yield of 4.02 g (70.9%). The synthesis employed a solvent mixture of dichloromethane and petroleum ether in a (1/8, v/v) ratio. ^{1}H NMR (400 MHz, Chloroform-d): δ 7.63 (s, 4H, Ar H), δ 7.49-7.55 (d, 4H, Ar H), δ 7.24-7.31 (t, 8H, Ar H), δ 7.11-7.17 (d, 12H, Ar H), δ 7.01-7.07 (t, 4H, Ar H); ^{13}C NMR (400 MHz, Chloroform-d): δ 147.69, 147.20, 139.03, 134.60, 129.30, 127.59, 126.39, 124.46, 123.93, 122.96.

2. Instruments and general methods

^{1}H NMR and ^{13}C NMR measurements were carried out on a Bruker Avance 400 spectrometer at resonant frequencies of 400 MHz or a JEOL JNM-ECZ500R/S1 spectrometer at resonant frequencies of 500 MHz, using Chloroform-d as solvent.

The crystallography data of DTPA2F and TPABTPA were collected by Rigaku-AFC11 equipped with a Rigaku Saturn CCD area detector (Bruker-SMART). The X-ray source was a graphic-monochromatized Mo-Kα radiation (λ = 0. 71073 Å) operating at 293 K under a flow of liquid nitrogen. Crystallographic data are available as supplementary publication numbers

CCDC 2357920 (DTPA2F) and 2357922 (TPABTPA) from the Cambridge Crystallographic Data Centre, which can be accessed free of charge at: www.ccdc.cam.ac.uk/data_request/cif.

Fourier-transform infrared (FT-IR) spectra were recorded with a Thermos Fisher Scientific iS50 spectrometers between 500 and 4000 cm^{-1}.

Thermal stability was assessed using thermogravimetric analyzer (TGA) operated at 10 °C min^{-1} from 30 to 600 °C under a nitrogen atmosphere on a METTLER TOLEDO TG/DSC 3+. Differential scanning calorimetry (DSC) analysis was conducted on a NETZSCH DSC214 at a heating rate of 10 °C min^{-1} under nitrogen atmosphere from 20 to 300 °C, with the glass transition temperature (T_g) determined from the midpoint of the thermal transition in the second heating cycle.

Ultraviolet-visible (UV-Vis) spectra were recorded on a 2600 UV-Vis spectrophotometer at room temperature.

Powder X-ray diffraction (PXRD) patterns were recorded by a Rigaku Mini Flex-II X-ray diffractometer with Cu-Kα radiation (λ = 1.54184 Å).

Scanning Electron Microscope (SEM) images were obtained by using Nova Nano SEM 230.

The photoluminescence quantum yield (PLQY) for crystalline powders was measured using a Horiba FluoroMax-4 spectrometer. The PLQY for DTPA2F in liquid and glass states was determined using a Hamamatsu Absolute PL Quantum Yield Spectrometer C11347 Quantaurus-QY, equipped with an integrating sphere (Hamamatsu, Japan).

Fabrication of DTPA2F transparent screen: The DTPA2F transparent screen was prepared using a simple melt-quenching technique. 800 mg of DTPA2F compound were placed in a beaker and heated to 160 °C until the material melted and all bubbles disappeared. The molten compound was then poured into a mold, and the DTPA2F transparent screen, with a square area of approximately 24 cm^2, was formed by natural cooling at room temperature.

Fabrication of organic scintillator films based on DTPA2F powders: An appropriate amount of the sample was ground for one hour. After grinding, 30 mg of the powder was dispersed in 500 mL of water using ultrasonication. A high-purity PET polyester microporous membrane with a pore size of 0.45 μm and a thickness of 11 μm was then placed in a 41 mm Büchner funnel. The turbid solution containing the sample was pumped through the filter for 5 hours. This process resulted in a flexible scintillator thin film with powder adhering to the PET membrane pores.

RL Intensity Measurements, X-Ray Photos Collection and Process: The RL spectra were measured by using a commercial miniature X-ray source, combined with an Edinburgh Fs5 fluorescence spectrophotometer (Edinburgh Instruments Ltd.). The X-ray source was a commercial miniature silver (Ag) target X-ray tube (AMPEK, Inc.), with a maximum tube current/power light output of 80 μA/4 W.

X-ray imaging measurement: X-ray photos were taken by a Cannon EOS 6D Mark II camera coupled with a commercial X-ray tube (tungsten target, Moxtek). All imaging tests are performed in a sealed lead box. By placing the samples between the X-ray source and the film with a distance of 3 cm (dose rate of 0.9 m Gy s^{-1}). Images were obtained by taking photographs through the scintillator film.[1]

3. Correlation formulas and analysis methods

The excited state energy levels and HOMO/LUMO orbitals were based on calculations via time-dependent density functional theory (TD-DFT)) and optimized at the b3lyp/6-31g(d) level. The calculations were performed with the Gaussian09 program. Visualization of the HOMO/LUMO orbitals was conducted using Multiwfn 3.8 and VMD.

Diffraction data were processed using the Crystal Clear 1.4.0 software, which includes symmetry-dependent data averaging and Lp-factor correction. The initial structural model of

the crystals was determined using the SHELXT program. Non-hydrogen atoms were identified based on difference Fourier peaks, and anisotropic refinement was applied to all non-hydrogen atoms. The positions of hydrogen atoms were determined using a theoretical hydrogenation procedure. Although all hydrogen atoms were considered in the structural calculations, they were not included in the structure refinement. Main structural refinement data for the resulting crystals are presented in Table S4.

The X-ray excited relative light yield was calculated as follows:

The X-ray attenuation efficiency (AE) was determined using the following formula

$$AE(\varepsilon,d) = \left(1 - e^{-c(\varepsilon)\rho d}\right) \times 100\% \qquad\qquad \text{Equation S1}$$

where $c(\varepsilon)$ is the photon cross section function obtained from the XCOM database of National Institute of Standards and Technology (NIST), ε is the photon energy, ρ is the density of scintillator and d is the thickness. In this study, the densities of the commercial BGO and Anthracene (An) crystals utilized were 7.13 g/cm^3 and 1.24 g/cm^3, respectively. We used a tablet press to tablet DTPA2F and TPABTPA powder, and obtained a round disc with a thickness of about 2 mm and a diameter of 1 cm. The disc densities of DTPA2F and TPABTPA after tableting were calculated to be 1.098 g/cm^3 and 1.097 g/cm^3, respectively. The DTPA2F powder was melted in the mold, and the density of DTPA2F glassy material was calculated to be 1.34 g/cm^3. For the calculation of the relationship between attenuation efficiency and scintillator thickness, we used a photon energy of 22 keV (the average energy of the X-ray tube) and a thickness of 2 mm. The mass absorption coefficients of BGO, An, DTPA2F and TPABTPA were 54.299 cm^2/g, 0.3949 cm^2/g, 0.4781 cm^2/g and 0.4336 cm^2/g, respectively. As shown in Figure S12a the attenuation efficiencies of BGO, An, DTPA2F, TPABTPA and DTPA2F-Glass calculated by the above formula are 100%, 9.33%, 9.12%, 8.31%, and 11.01%, respectively.

$$PC_{normalized} = \frac{PC_{measured}}{AE(d)}$$
Equation S2

where AE (d) is the attenuation coefficient at the actual thickness.

The actual light yield of the sample LY_{sample} is defined as:

$$LY_{sample} = LY_{reference}\frac{PC_{normalized}(sample)}{PC_{normalized}(reference)}$$
Equation S3

where $LY_{reference}$ is the light yield of BGO (8000 photons MeV^{-1})[2], PC (Photon Counting) is the RL spectral integral area of the unknown material, and $AE(\%)$ is the attenuation efficiency after pressing. The relative light yield under X-ray excitation is determined using the method described in the literature,[3] and the relative light yields obtained in this study are comparable to the steady-state X-ray-light internal conversion efficiencies of the reference BGO sample. The RL spectral integral areas for BGO, Anthracene, DTPA2F, TPABTPA, and DTPA2F-Glass are shown in Figure S12b. and the radiant peak areas of the above materials are integrated respectively. the radiant integral areas of BGO, An, DTPA2F, TPABTPA and DTPA2F-Glass are 45916486, 8589089, 24288323, 11469090 and 18105318, respectively. In addition, the error bars were determined by the measurements of three samples and each sample was measured three times. The integration of the three test results was processed, and the difference of the integral area was 0.875%. Small differences in the intensity of radiation emission caused by the instrument lead to slight differences in the calculation of light yield. Next, the relative method is used to calculate by Equation S3

Such as: $LY_{DTPA2F} = LY_{BGO}\ PC_{DTPA2F}/PC_{BGO} = 8000 \times [24288323/(9.12 \pm 0.875\%)]/(45916486/100\%) \approx 46400 \pm 406$ photons MeV^{-1}。

Using the same method, the light yields of TPABTPA and DTPA2F-Glass are (24056 ± 209) and (28341 ± 246) photons MeV^{-1}, respectively. The light yield of anthracene, calculated using

BGO as the reference, is 16035 ± 140 photons MeV^{-1}, which closely matches its standard value of 15900 photons MeV^{-1}, confirming the accuracy of the light yield measurements.

The detection limit is calculated according to Equation S4.

$$LOD = \frac{3\sigma}{slope}$$

Equation S4

where σ is the instrumental average noise and slope is the slope of the fitted line. As shown in Figure S13d, we measured the corresponding radiation luminescence intensity under different doses. By linear fitting of the relationship between radiation dose and radiation intensity, the corresponding slopes of DTPA2F, DTPA2F-Glass and TPABTPA are 1656, 1169 and 713,respectively. At the same time, the average intensity of blank background is about 20.9 (a. u) when no sample is placed. Select the signal-to-noise ratio of 3 for calculation, and substitute the test background value and fitting slope into Equation S4 for calculation. The detection limits of DTPA2F, DTPA2F-Glass and TPABTPA were 37.9, 53.7, 87.9 nGy s $^{-1}$, respectively.

DTPA2F and TPABTPA powders were analyzed using the FLS980 spectrometer with excitation at 450 nm, and the fluorescence decay times were calculated using Equation S5:

$$I(t) = I_0 + A_1 e^{-\frac{t}{\tau_1}}$$

Equation S5

where $I(t)$, I_0 and A_1 are the photoluminescence intensity at time, background and amplitude, respectively.

The non-radiative transition rate is calculated by Equation S6:

$$k(nr) = \frac{1 - \Phi_f}{\tau_1}$$

Equation S6

where Φ_f is the PLQY and τ is the lifetime.

The spatial resolution of X-ray imaging was determined using Modulation Transfer Function (MTF) measurements. The line-pair card captured in the X-ray image was analyzed using

ImageJ software to obtain a curve of pixel intensity versus pixel position. MTF was then calculated using Equation S7. To further refine the resolution measurement, the slanted edge method was applied. Sharp-edge X-ray imaging was conducted on a standard tungsten sheet with an approximate thickness of 0.5 mm. The MTF was computed using ImageJ software，first, the edge spread function (ESF) was derived from the edge image, then the line spread function (LSF) was obtained by differentiating the ESF. Finally, the MTF was defined as the Fourier transform of the LSF, as described in Equation S8:

$$MTF = \frac{I_{max} - I_{min}}{I_{max} + I_{min}}$$

Equation S7

where I_{min} and I_{max} are the minimum and maximum values of the function used to quantify the contrast, respectively.

$$MTF(v) = F[LSF(x)] = F\left[\frac{dLSF(x)}{dx}\right]$$
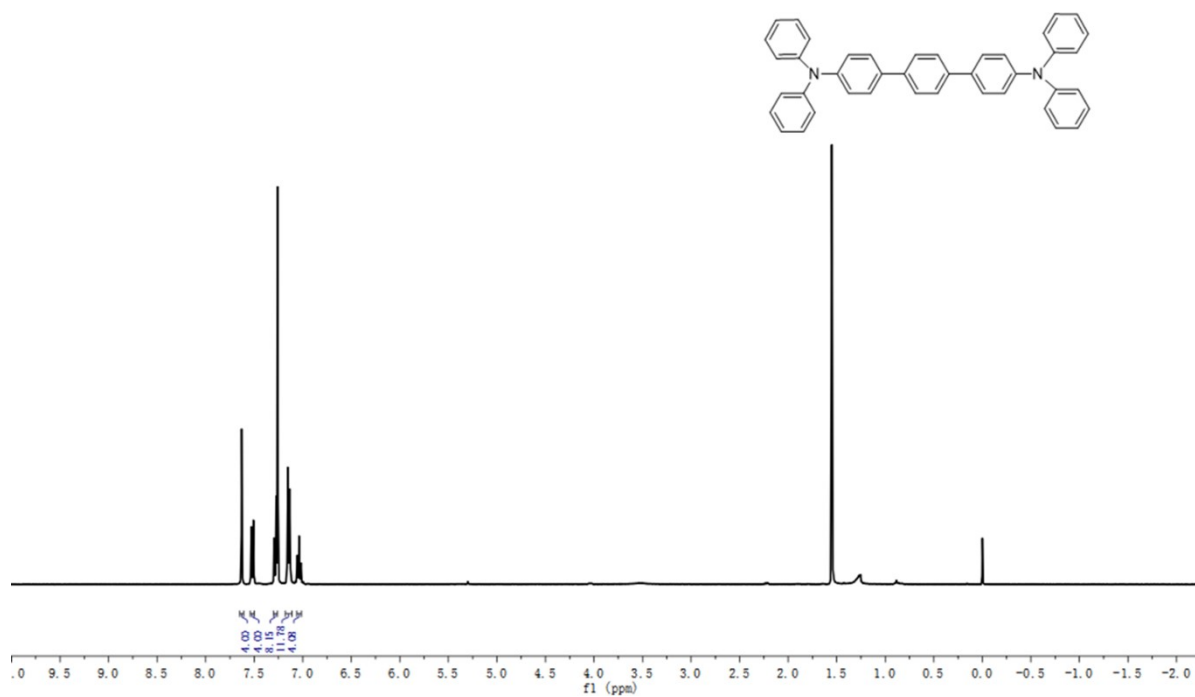
Equation S8

where v was the spatial frequency and x is the position of pixels.
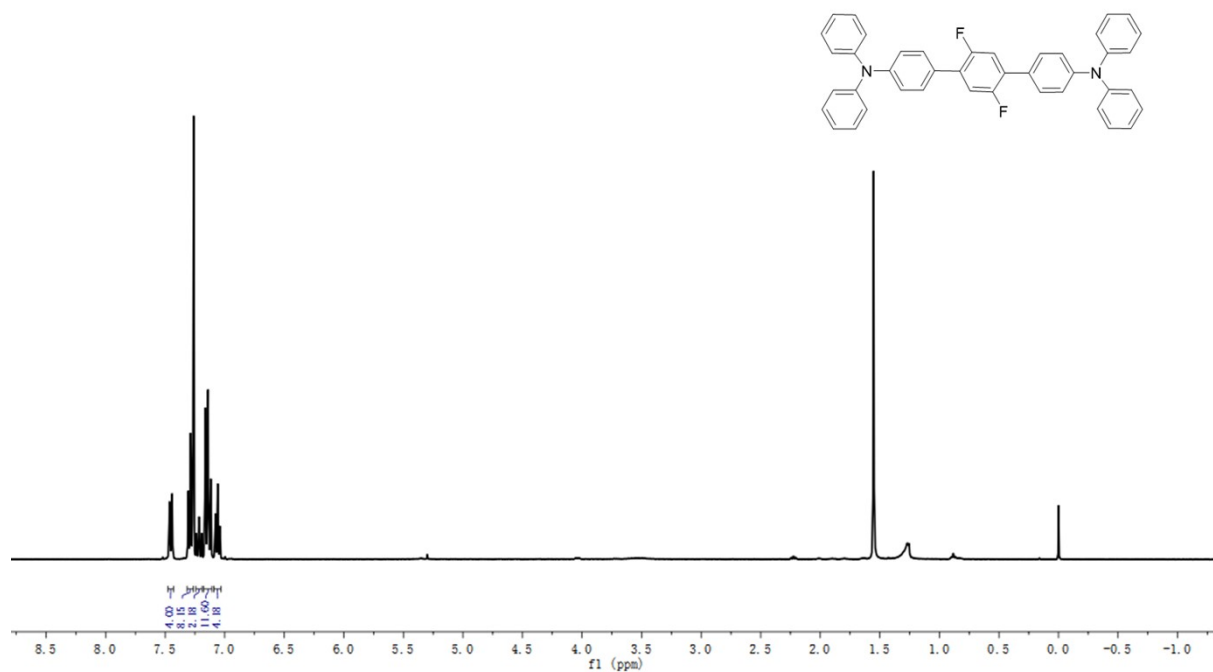
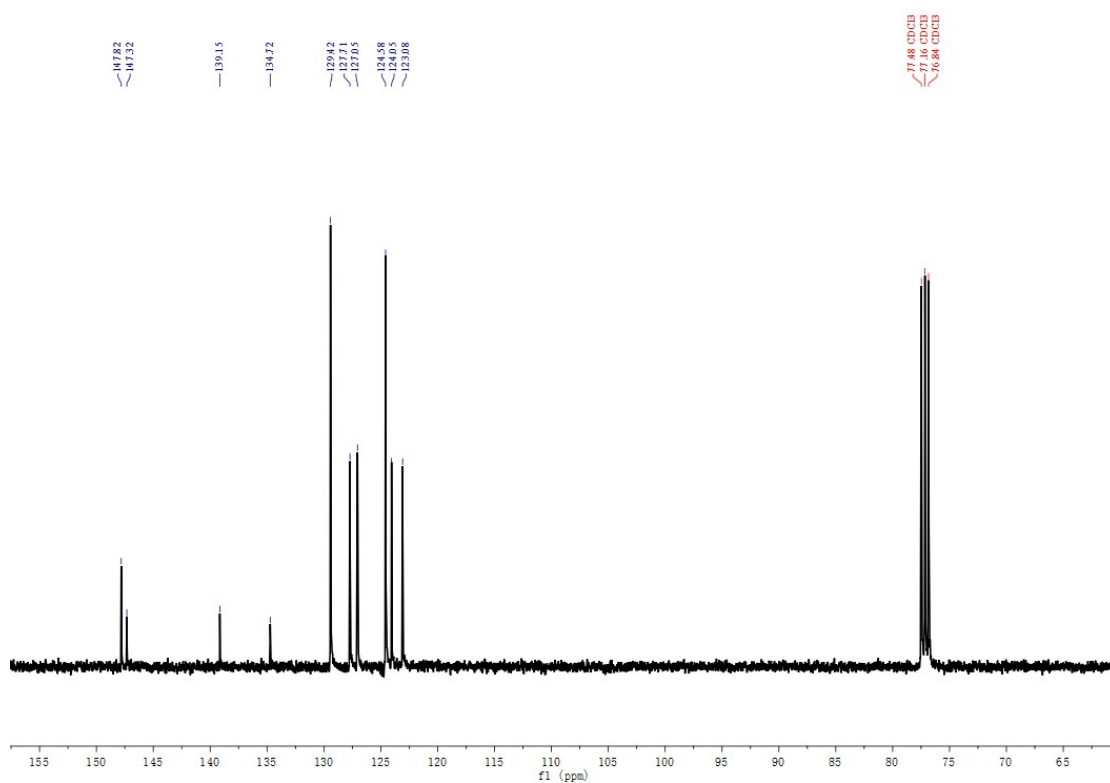**Figure S3.** ^{1}H NMR spectrum of DTPA2F in CDCl$_3$ (25 °C, 400 MHz).
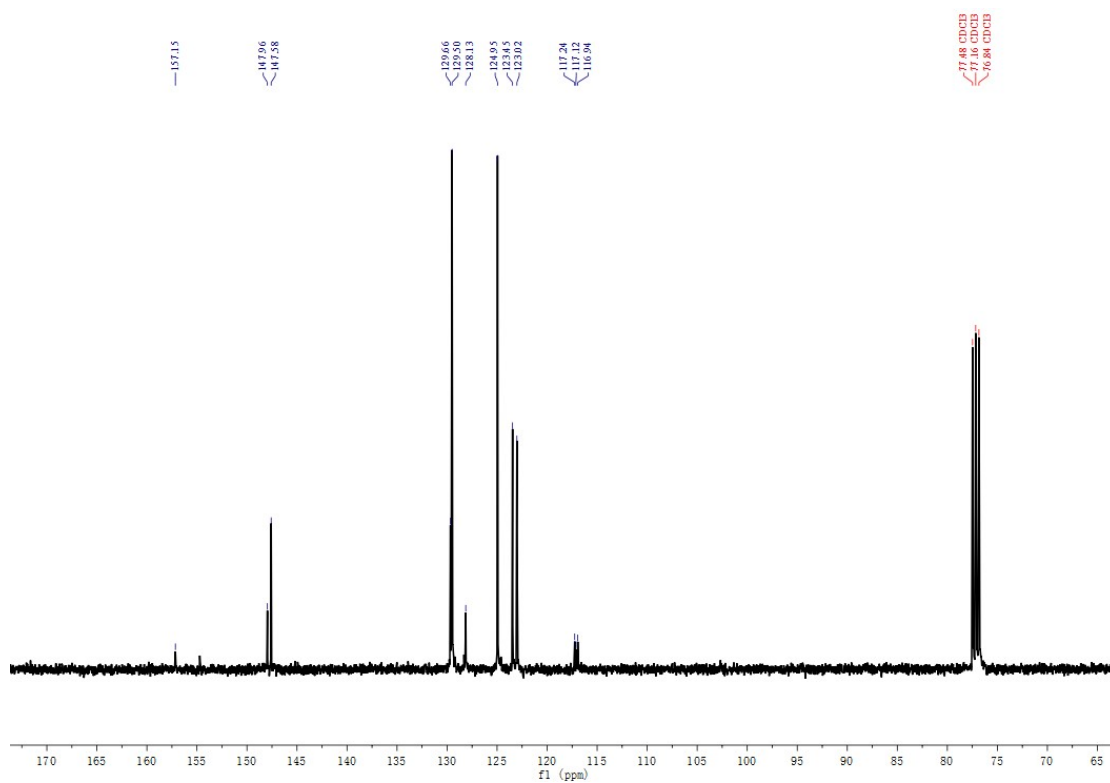
**Figure S4.** ^{13}C NMR spectrum of DTPA2F in CDCl$_3$ (25 °C, 400 MHz).

Figure S5. ^{1}H NMR spectrum of TPABTPA in CDCl$_3$ (25 °C, 400 MHz).

Figure S6. ^{13}C NMR spectrum of TPABTPA in CDCl$_3$ (25 °C, 400 MHz).

Table S1. Distribution of singlet and triplet energy levels and corresponding spin-orbit coupling constants of DTPA2F and TPABTPA molecules.

Singlet	DTPA2F (eV)	TPABTPA (eV)	Triplet	DTPA2F (eV)	TPABTPA (eV)	SOC (cm^{-1})	DTPA2F	TPABTPA
S_1	3.1776	3.3021	T_1	1.7915	2.6295	$\xi(S_1,T_1)$	0.0806	0.1556
S_2	3.4788	3.6017	T_2	2.5426	2.9453	$\xi(S_1,T_2)$	0	0
S_3	3.8694	3.8402	T_3	3.1492	3.1744	$\xi(S_1,T_3)$	0.7090	0.7901
S_4	3.8727	3.8449	T_4	3.1493	3.1745	$\xi(S_1,T_4)$	0.0100	0.0100
S_5	4.0472	4.0305	T_5	3.2067	3.4662	$\xi(S_1,T_5)$	0.4500	0.5548

(a)   (b)
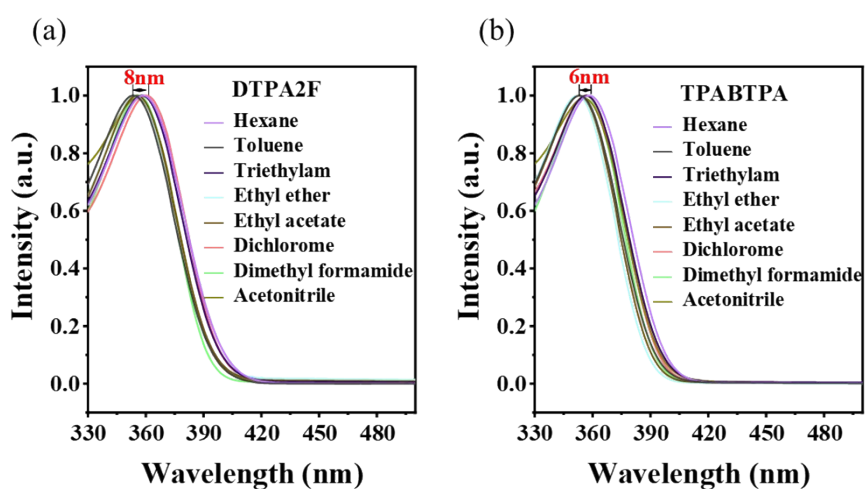
Figure S7. UV-vis absorption spectra in different solvents with varied polarities of (a) DTPA2F and (b) TPABTPA (1×10^{-5} mol L^{-1}).

Table S2. The detailed absorption and emission data of DTPA2F in different solvents.

Solvents	ε	n	$f(\varepsilon, n)$	λ_A (nm)	λ_{PL} (nm)	ν_A-ν_{PL} (cm^{-1})

Solvents	ε	n	$f(\varepsilon, n)$	λ_A (nm)	λ_{PL} (nm)	$\nu_A-\nu_{PL}$ (cm^{-1})
Hexane	1.90	1.375	0.0012	356	408	3580.083718
Toluene	2.38	1.494	0.013	360	414	3623.188405
Triethylamine	2.42	1.401	0.048	355	414	4014.424712
Isopropyl ether	3.88	1.368	0.145	356	422	4393.205175
Ethyl ether	4.34	1.352	0.167	355	421	4416.044963
Ethyl acetate	6.02	1.372	0.200	355	431	4967.157936
Dichloromethane	8.93	1.424	0.217	358	443	5359.597462
Dimethylformamide	37.0	1.427	0.276	359	456	5925.328641
Acetonitrile	37.5	1.344	0.3053	353	468	6961.090530

Table S3. The detailed absorption and emission data of TPABTP in different solvents.

Solvents	ε	n	$f(\varepsilon, n)$	λ_A (nm)	λ_{PL} (nm)	$\nu_A-\nu_{PL}$ (cm^{-1})
Hexane	1.90	1.375	0.0012	356	399	3027.230998
Toluene	2.38	1.494	0.013	357	406	3380.662609
Triethylamine	2.42	1.401	0.048	355	404	3416.538836
Isopropyl ether	3.88	1.368	0.145	351	407	3920.003920
Ethyl ether	4.34	1.352	0.167	352	412	4137.246248
Ethyl acetate	6.02	1.372	0.200	352	415	4451.566951
Dichloromethane	8.93	1.424	0.217	357	424	4426.298821
Dimethylformamide	37.0	1.427	0.276	358	436	4997.181077
Acetonitrile	37.5	1.344	0.3053	356	437	5206.592445
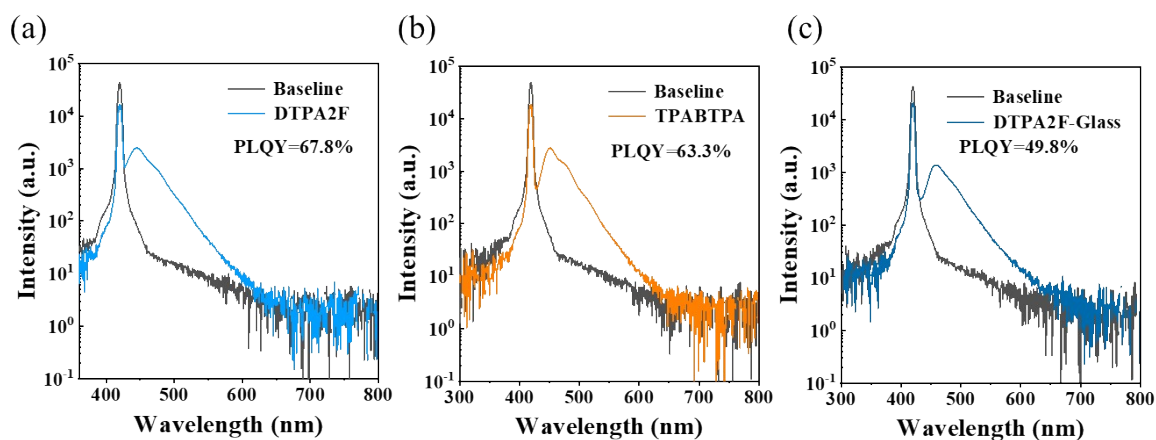
Figure S8. Photoluminescence quantum yield of (a) DTPA2F powders, (b) TPABTPA powders and (c) DTPA2F-Glass.
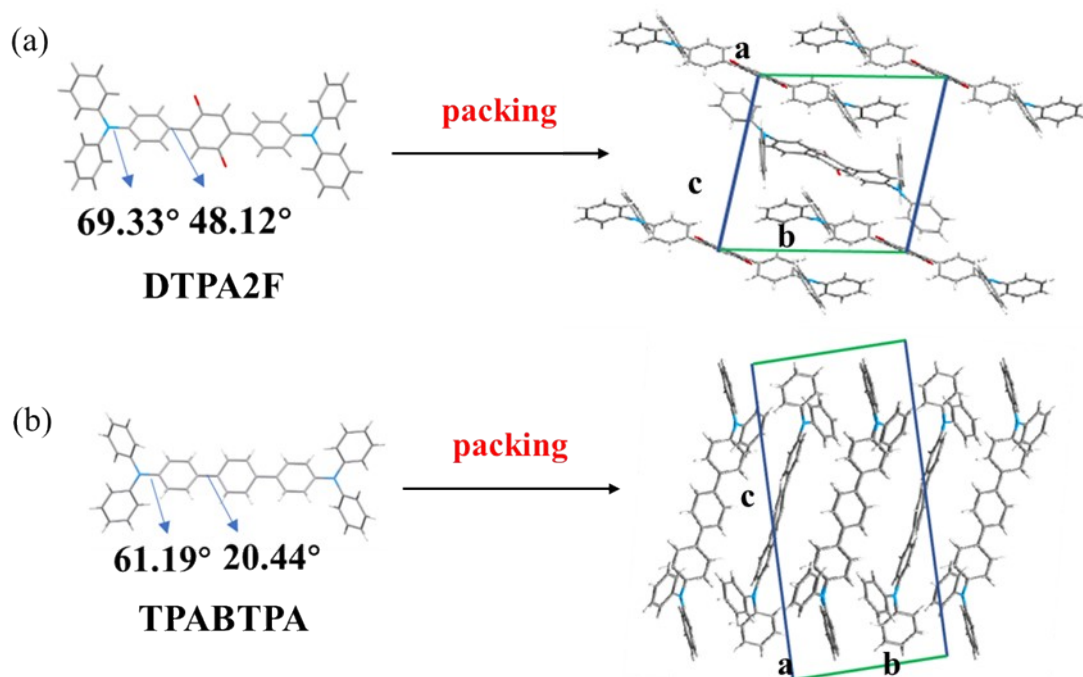
**Figure S9**. Crystal structures and stacking mode of molecules of (a) DTPA2F and (b) TPABTPA.

Table S4. The crystallographic data of compounds DTPA2F and TPABTPA.

Complex	DTPA2F	TPABTPA
Empirical formula	$C_{42}H_{30}N_2F_2$	$C42H_{32}N_2$, $(CHCl_2)$
Formula weight	600.68	649.62
Temperature/K	296.15	296.15
Crystal system	Triclinic	Triclinic
Space group	P-1	P-1
a/Å	10.0731(4)	7.876(8)
b/Å	12.6282(6)	10.166(5)
c/Å	12.9970(6)	21.176(13)
α/°	100.540(4)	78.16(5)
β/°	105.121(4)	85.41(5)
γ/°	91.458(4)	86.98(5)
Volume/Å^3	1564.45(13)	1653(2)
Z	4	2
ρca lcg/cm^3	1.275	1.305
μ/mm^{-1}	0.082	2.022

F(000)	628	680.0
Crystal size/mm^3	0.2 × 0.2 × 0. 2	0.2 × 0.2 × 0.2
Radiation		
2Θ range for data collection/°	4.708 to 58.558	8.554 to 145.746
Index ranges	-13 ≤ h ≤ 13, -15 ≤ k ≤ 17, -17 ≤ l ≤ 17	-8 ≤ h ≤ 9, -12 ≤ k ≤ 12, -26 ≤ l ≤ 26
Reflections collected	4982 1462	12758 6128
Independent reflections	R_{int} = 0.0323, R_{sigma} = 0.0430	R_{int} = 0.0598, R_{sigma} = 0.0778
Data/restraints/parameters	7329/0/415	6128/0/397
Goodness-of-fit on F^2	1.028	1.035
R_1[a], wR_2[b] [I≥2σ (I)]	R_1 = 0.0472, wR_2 = 0.1040	R_1 = 0.0739, wR_2 = 0.1962
R_1[a], wR_2[b] [all data]	R_1 = 0.0905, wR_2 = 0.1187	R_1 = 0.0971, wR_2 = 0.2238
Largest diff. peak/hole / e Å^{-3}	0.14/-0.18	0.35/-0.39

[a] $R_1 = \sum||F_0| - |F_c||/\sum|F_0|$, [b] $wR_2 = [\sum w(F_0^{\ 2} - F_c^{\ 2})^2 /\sum w(F_0^{\ 2})]^{1/2}$.
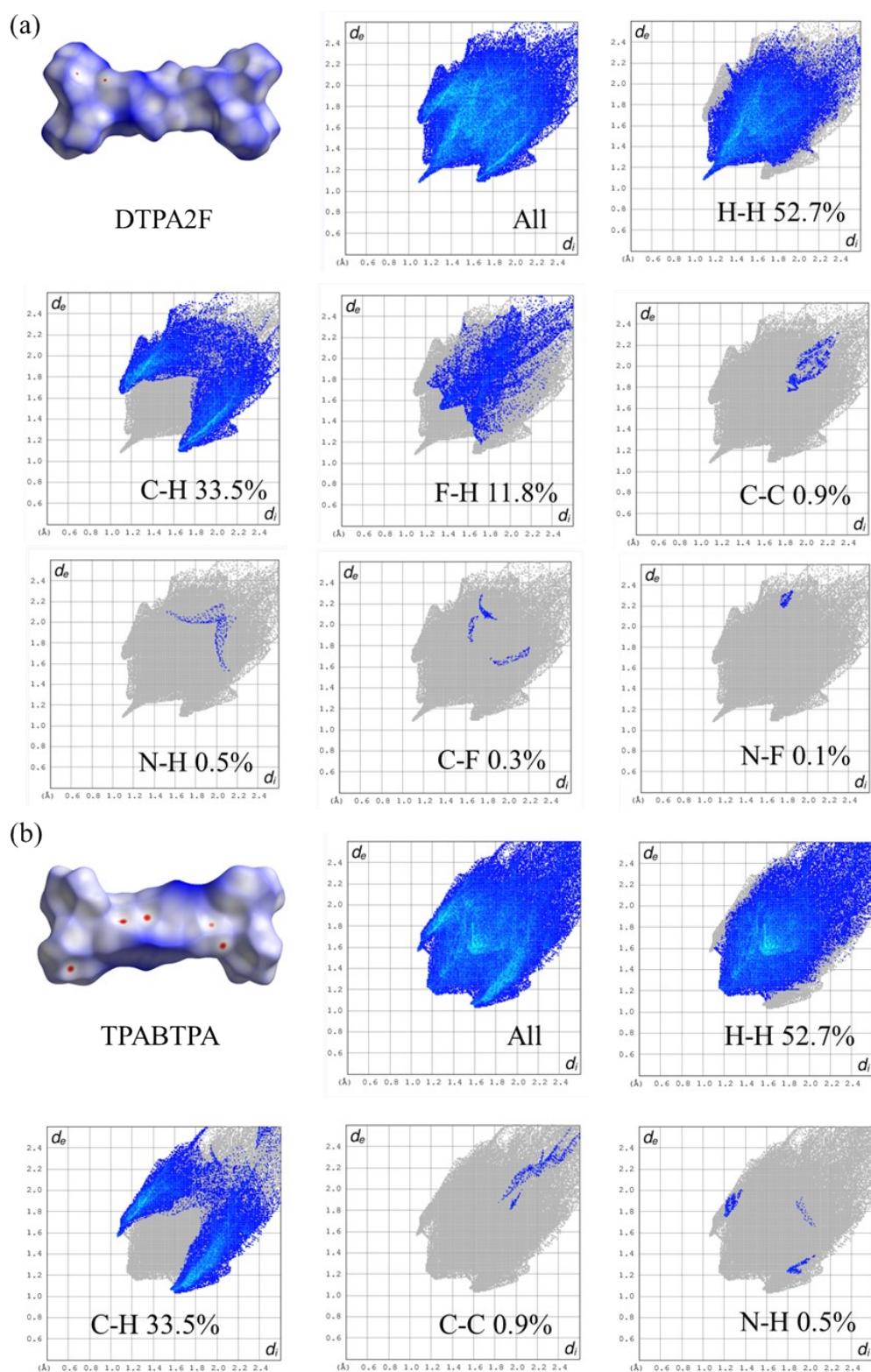
Figure S10. Hirshfeld surfaces analysis of (a) DTPA2F and (b) TPABTPA mapped with d_{norm} over the range −0.17 to 1.56. Close contacts are shown red on the surface. Two-dimensional fingerprint plots of crystals calculated from the Hirshfeld surfaces.
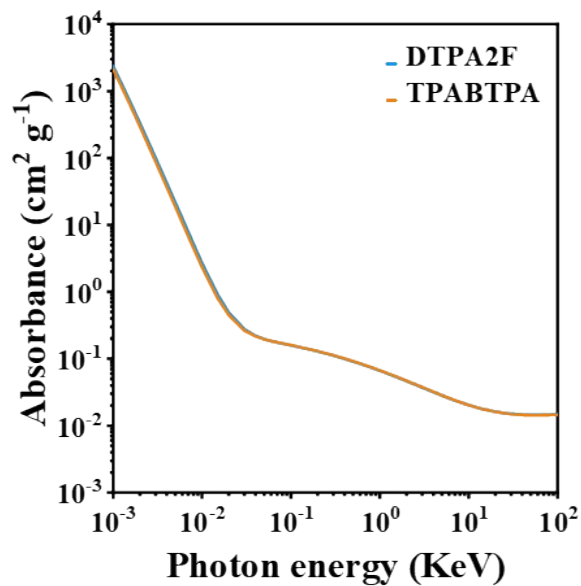
Figure S11. X-ray absorption spectra of DTPA2F (blue line) and TPABTPA (orange line) measured as a function of X-ray energy. The attenuation coefficient μ was obtained from the photon cross-section database.
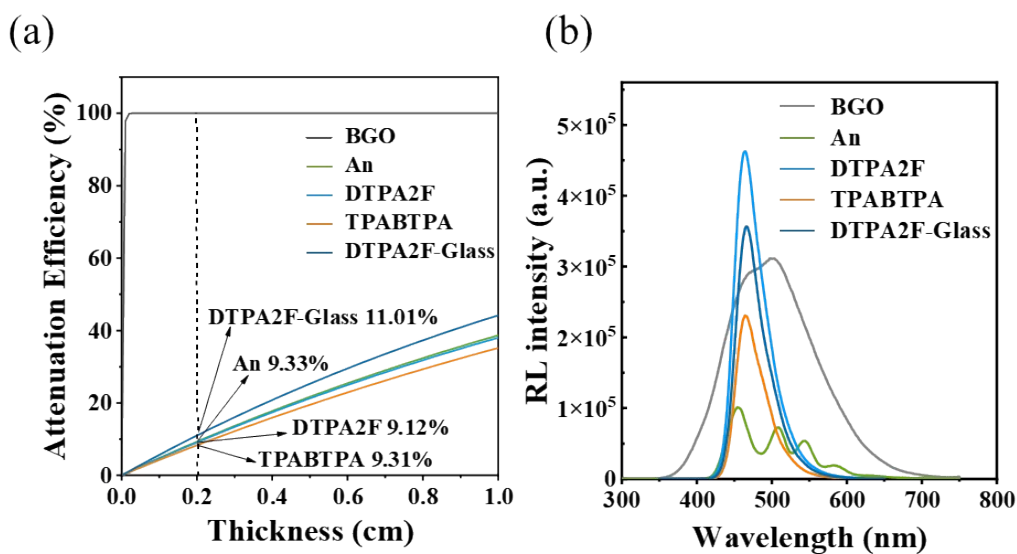

Figure S12. (a)The attenuation efficiency curve of BGO, Anthracene, DTPA2F, TPABTPA, DTPA2F-Glass. (b) The RL intensity curve of BGO, Anthracene (An), DTPA2F, TPABTPA, DTPA2F-Glass.
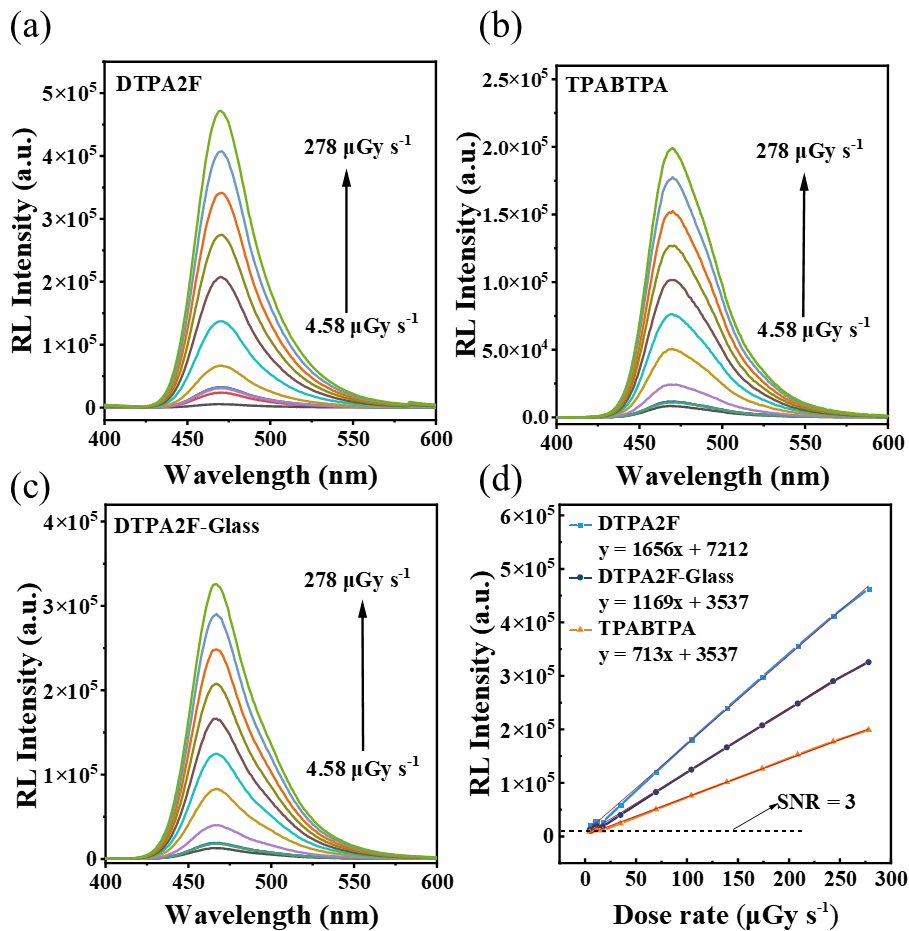
Figure S13. The RL intensity of (a) DTPA2F powders, (b) TPABTPA powders and (c) DTPA2F-Glass (under the X-ray dose rates range from 4.58 to 278 μ Gy s^{-1}). (d)Fitted detection limits of DTPA2F, TPABTPA and DTPA2F-Glass
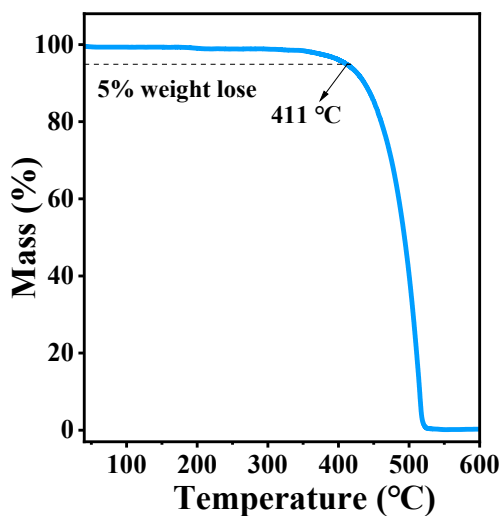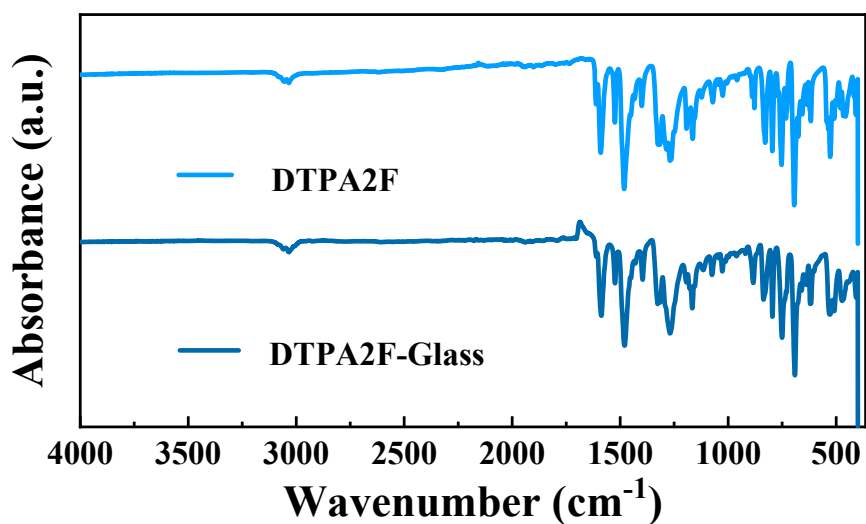

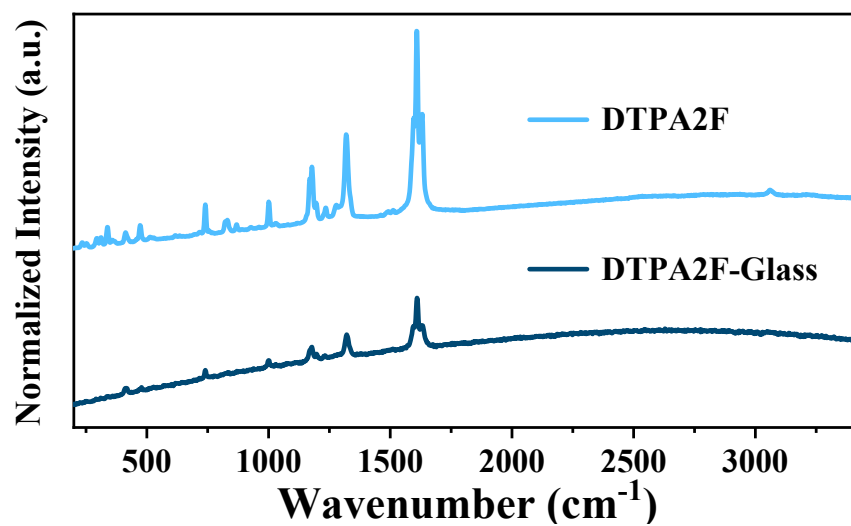**Figure S14.** The TGA curves of DTPA2F powders.
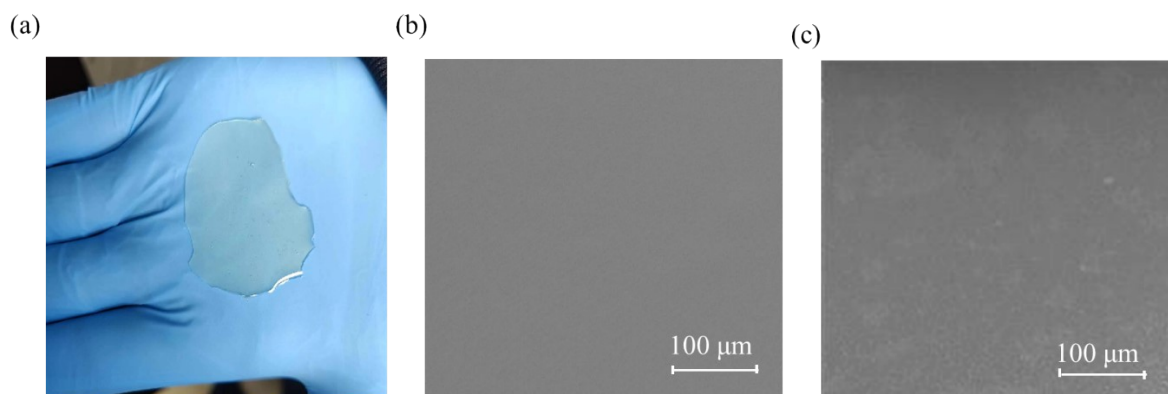
Figure S15. (a) The DTPA2F-Glass film under daylight (b) SEM image of newly prepared DTPA2F-glass film (c) SEM images of DTPA2F-glass film placed over 100 days.
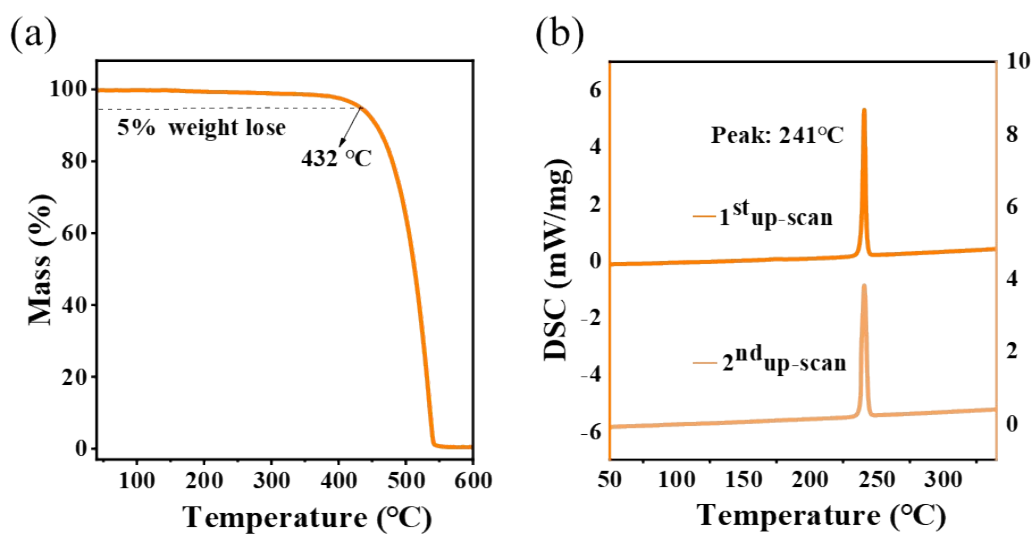
**Figure S16.** (a) The TGA and (b) DSC curves of TPABTPA.

**Figure S17.** The FT-IR spectra of DTPA2F powder and DTPA2F-Glass film.

Figure S18. The Raman spectra of DTPA2F powder and DTPA2F-Glass film.

Table S5. Comparison of related parameters between DTPA2F glassy materials and some reported metal halide glassy materials.

Sample (Glass state)	Transparency	Light Yield (photons MeV^{-1})	Spatial Resolution (lp mm^{-1})	PLQY of Crystal (%)	PLQY of Glass (%)	Decay time	Ref.
DTPA2F	>87% @450-800 nm	28341	38.5	67.8	49.8	1.62 ns	This work
$(C_{20}H_{20}P)_2SbCl_5$	>80% @450-800 nm	12535	30.0	86.6	44.5	3.58 μs	4
$(ETP)_2MnBr_4$	>80% @500-800 nm	35000	13.4	-	-	295 μs	5
$(DPG)_2MnBr_4$	>75% 554-800 nm	2700	10.0	41.0	13.7	235 μs	6
$(DOTG)_2MnBr_4$	>80% 512-800 nm	3000	12.0	87.0	28.0	187 μs	6
$(MTP)_2Cu_4I_6-\beta$	-	700	-	89.0	2.0	1.00 μs	7
$(HTPP)_2MnBr_4$	>78% @506-800 nm	8600	10.0	98.6	28.5	190 μs	3
$[CH_3Ph_3P]_2MnBr_4$	>80% @505-700 nm	12570	12.3	83.5	47.8	193 μs	8
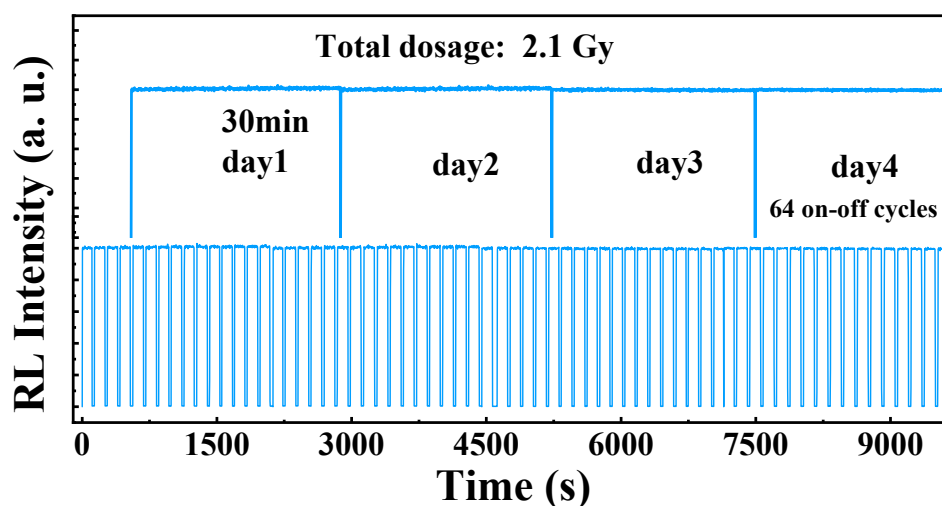
Figure S19. The emission stability under continuous irradiation 4 days (30 min per day) for the DTPA2F glass at a dose rate of 278 μGy s^{-1}.
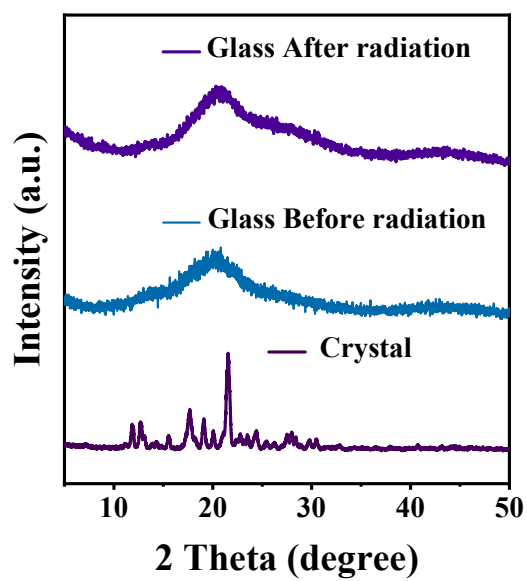
Figure S20. DTPA2F-Glass compared with before and after radiation PXRD pattern.
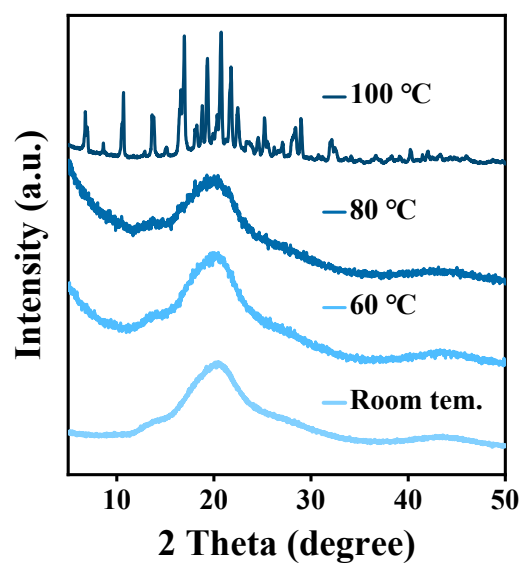

Figure S21. DTPA2F-Glass compared with Different heating temperature radiation PXRD pattern.

Table S6. Performance comparison of organic scintillators for X-ray imaging reported in literature.

Sample	Composition	Resolution (lp mm^{-1})	Decay time	Ref.
DTPA2F	Glass state	38.5	1.66 ns	This work
9.10-DPA	Single crystal	20	1.63 ns	9
DMAc-TRZ	0.5 wt% in SO	16.6	2170 ns	10
Py2TTZ-I$_2$F$_4$	100 wt% in PET	26.8	1.44 ns	11
BIC	5 wt% in PDMS	16.7	2.71 ns	12
CBP	PDMS	14.3	1.15 ns	13
PAM-M4	Glass state	27	12.38 ns	14
DCB@C[3]A	100 wt% in PET	20	3749 ns	15
D-A$_{0.5}$	5 wt% in PSF	27.5	1190 ns	16
C4-I	50 wt% CL	>14.3	443.75 μs	17
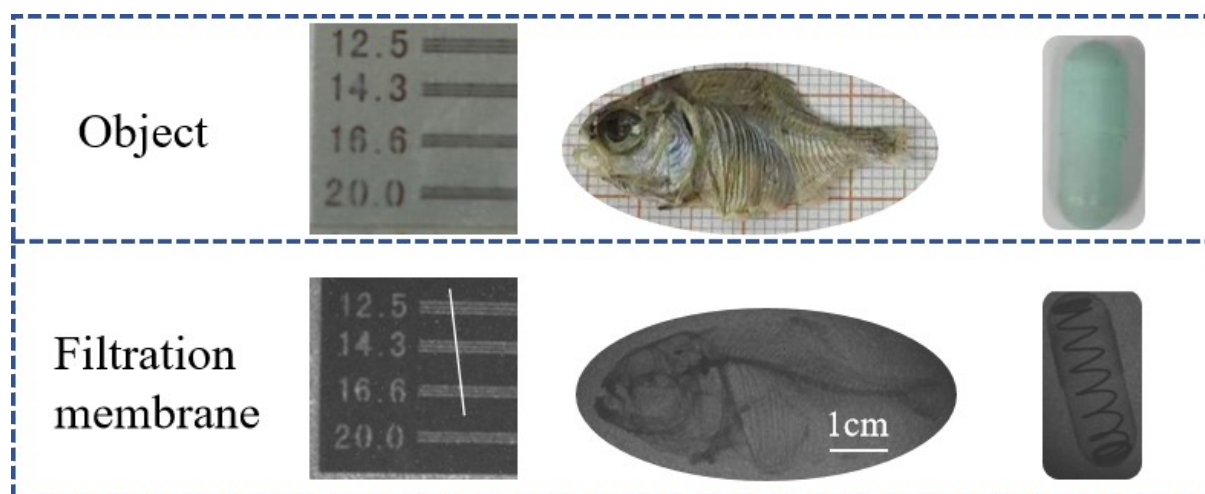
Figure S22. The spatial resolution of the digital X-ray imaging is measured by a line pair card, fish and with metal spring capsule of organic scintillator films based on DTPA2F.
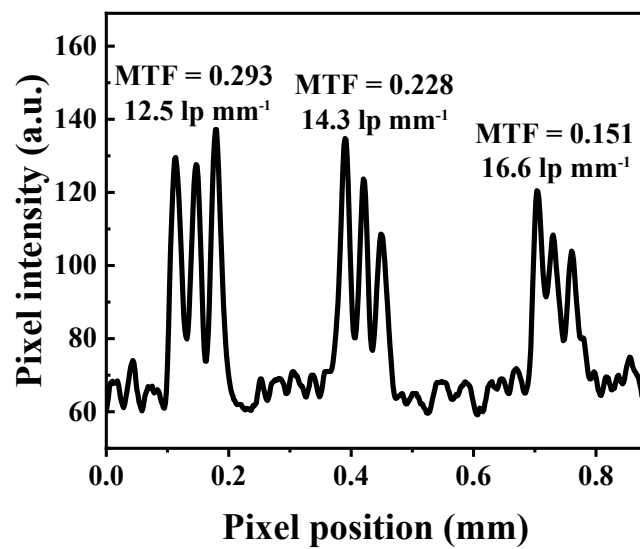
Figure S23. The pixel intensity versus pixel positions, resolution from 12.5 to 16.6 lp mm^{-1} based on the white line in Figure S22.

References

1. J.-X. Wang, L. Gutiérrez-Arzaluz, X. Wang, T. He, Y. Zhang, M. Eddaoudi, O. M. Bakr and O. F. Mohammed, Heavy-atom engineering of thermally activated delayed fluorophores for high-performance X-ray imaging scintillators, *Nat. Photon.*, 2022, **16**, 869-875.

2. W. Li, Y. Li, Y. Wang, Z. Zhou, C. Wang, Y. Sun, J. Sheng, J. Xiao, Q. Wang, S. Kurosawa, M. Buryi, D. John, K. Paurová, M. Nikl, X. OuYang and Y. Wu, Highly Efficient and Flexible Scintillation Screen Based on Organic Mn(II) Halide Hybrids toward Planar and Nonplanar X‑Ray Imaging, *Laser Photonics Rev.*, 2023, **18**, 2300860.

3. J. B. Luo, J. H. Wei, Z. Z. Zhang, Z. L. He and D. B. Kuang, A Melt‑Quenched Luminescent Glass of an Organic–Inorganic Manganese Halide as a Large‑Area Scintillator for Radiation Detection, *Angew. Chem. Int. Ed.*, 2023, **62**, e202216504.

4. T. Feng, Z. a. Zhou, Y. n. An, L. Chen, Y. Fu, S. Zhou, N. Wang, J. Zheng and C. Sun, Large-Area Transparent Antimony-Based Perovskite Glass for High-Resolution X-ray Imaging, *ACS Nano*, 2024, **18**, 16715-16725.

5. B. Li, Y. Xu, X. Zhang, K. Han, J. Jin and Z. Xia, Zero‑Dimensional Luminescent Metal Halide Hybrids Enabling Bulk Transparent Medium as Large‑Area X‑Ray Scintillators, *Adv. Opt. Mater.*, 2022, **10**, 2102793.

6. Z. L. He, J. H. Wei, J. B. Luo, Z. Z. Zhang, J. H. Chen, X. X. Guo and D. B. Kuang, Guanidinium‑Based Manganese(II) Bromide with High Glass‑Forming Ability for Thermoplastic Curved X‑ray Imaging, *Laser Photonics Rev.*, 2024, **18**, 2301249.

7. B. Li, J. Jin, X. Liu, M. Yin, X. Zhang, Z. Xia and Y. Xu, Multiphase Transformation in Hybrid Copper(I)-Based Halides Enable Improved X-ray Scintillation and Real-Time Imaging, *ACS Mater. Lett.*, 2024, **6**, 1542-1548.

8. Z. Z. Zhang, Z. L. He, J. B. Luo, J. H. Wei, X. X. Guo, J. H. Chen and D. B. Kuang, Organic–Inorganic Hybrid Mn‑Based Transparent Glass for Curved X‑Ray Scintillation Imaging, *Adv. Opt. Mater.*, 2023, **12**, 2302434.

9. M. Chen, L. Sun, X. Ou, H. Yang, X. Liu, H. Dong, W. Hu and X. Duan, Organic Semiconductor Single Crystals for X‑ray Imaging, *Adv. Mater.*, 2021, **33**, 2104749.

10. W. Ma, Y. Su, Q. Zhang, C. Deng, L. Pasquali, W. Zhu, Y. Tian, P. Ran, Z. Chen, G. Yang, G. Liang, T. Liu, H. Zhu, P. Huang, H. Zhong, K. Wang, S. Peng, J. Xia, H. Liu, X. Liu and Y. M. Yang, Thermally activated delayed fluorescence (TADF) organic molecules for efficient X-ray scintillation and imaging, *Nat. Mater.*, 2021, **21**, 210-216.

11. Y.-H. Chen, G.-Z. Zhang, F.-H. Chen, S.-Q. Zhang, X. Fang, H.-M. Chen and M.-J. Lin, Halogen-bonded charge-transfer co-crystal scintillators for high-resolution X-ray imaging, *Chem. Sci.*, 2024, **15**, 7659-7666.

12. Q. Sun, H. Wang, J. Li, F. Li, W. Zhu, X. Zhang, Q. Chen, H. Yang and W. Hu, Nano Organic Co‑Crystal Scintillator for X‑ray Imaging, *Small Structures*, 2023, **4**, 2200275.

13. H. Chen, M. Lin, C. Zhao, D. Zhang, Y. Zhang, F. Chen, Y. Chen, X. Fang, Q. Liao, H. Meng and M. Lin, Highly Efficient, Low‑Dose, and Ultrafast Carbazole X‑Ray Scintillators, *Adv. Opt. Mater.*, 2023, **11**, 2300365.

14. X. Quan, G. Z. Zhang, Y. Zhang, Q. Liao, H. M. Chen and M. J. Lin, Low‑Cost, Large‑Area, and Highly Transparent Organic Glassy Scintillators for High Resolution X‑Ray Imaging, *Adv. Opt. Mater.*, 2024, **12**, 2400113.

15. G. Zhang, F. Chen, Y. Di, S. Yuan, Y. Zhang, X. Quan, Y. Chen, H. Chen and M. Lin, Guest‑Induced Thermally Activated Delayed Fluorescence Organic Supramolcular Macrocycle Scintillators for High‑Resolution X‑Ray Imaging, *Adv. Funct. Mater.*, 2024, DOI: 10.1002/adfm.202404123.

16. J. X. Wang, J. Yin, L. Gutiérrez‑Arzaluz, S. Thomas, W. Shao, H. N. Alshareef, M. Eddaoudi, O. M. Bakr and O. F. Mohammed, Singlet Fission‑Based High‑Resolution X‑Ray Imaging Scintillation Screens, *Adv. Sci.*, 2023, **10**, 2300406.

17. J.-H. Wei, J.-B. Luo, Z.-L. He, Q.-P. Peng, J.-H. Chen, Z.-Z. Zhang, X.-X. Guo and D.-B. Kuang, Phosphonium Iodide Featuring Blue Thermally Activated Delayed Fluorescence for Highly Efficient X‑ray Scintillator, *Angew. Chem. Int. Ed.*, 2024, DOI: 10.1002/anie.202410514.